Volume 27
Number 1
7 January 2025
Pages 1–610

PCCP

Physical Chemistry Chemical Physics

rsc.li/pccp

25 YEARS ANNIVERSARY

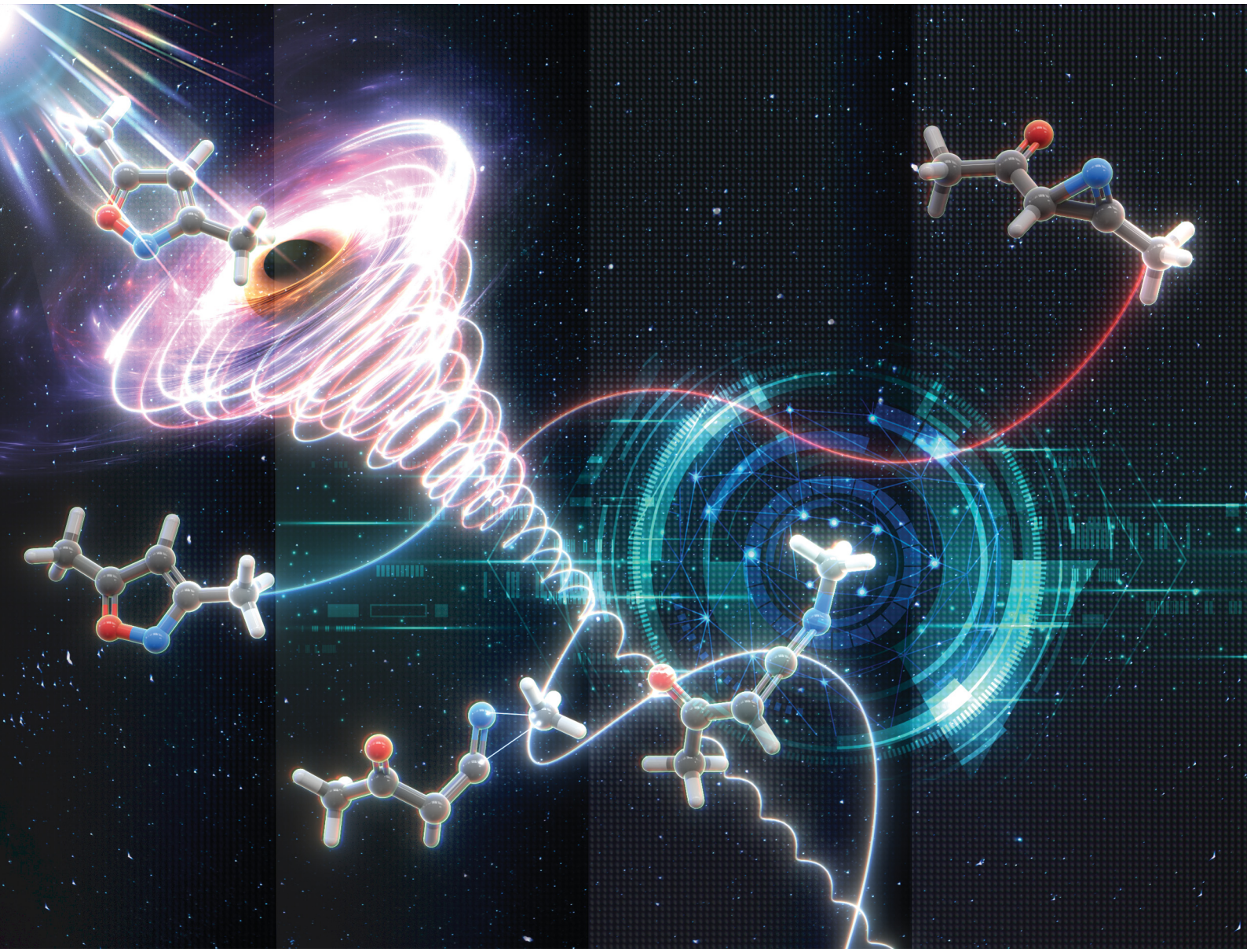

ISSN 1463-9076

ROYAL SOCIETY OF CHEMISTRY

PAPER

Mizuki Kimura and Shinkoh Nanbu

Nonadiabatic *ab initio* chemical reaction dynamics for the photoisomerization reaction of 3,5-dimethylisoxazole *via* the S_1 electronic state

PCCP Owner Societies

PCCP

ROYAL SOCIETY OF CHEMISTRY

PAPER

View Article Online
View Journal | View Issue

Cite this: *Phys. Chem. Chem. Phys.*, 2025, **27**, 62

Nonadiabatic *ab initio* chemical reaction dynamics for the photoisomerization reaction of 3,5-dimethylisoxazole *via* the S_1 electronic state†

Mizuki Kimura[a] and Shinkoh Nanbu *[b]

Received 8th August 2024,
Accepted 4th November 2024

DOI: 10.1039/d4cp03137g

rsc.li/pccp

Nonadiabatic *ab initio* molecular dynamics simulations were performed to explore the photoisomerization pathway from isoxazole (iso-OXA) to oxazole (OXA), considering four electronic states. The XMS-CASPT2 and SA4-CASSCF theories were employed to describe these electronic structures, which were caused by 12 electrons in 11 orbitals with the cc-pVDZ + sp diffuse basis set; the Gaussian s- and p-type diffuse functions were extracted from Dunning's aug-cc-pVDZ function. The potential energy and its gradient at each time step were computed on-the-fly at these levels in the time evolution of the classical trajectory. When the two electronic states were close to each other, the trajectory surface hopping (TSH) judgment between the two adjacent states was carried out by the anteater procedure based on the Zhu–Nakamura formula (ZN-TSH). The two different excited state lifetimes were found to exist in the first electronic state (S_1), estimated at 10.77 and 119.81 fs. Upon photoexcitation, the N–O bond breaks and energetically relaxes to the ground state (S_0). In the pathway leading to the main product, azirine formation, the 5-membered ring retains a planar structure while undergoing a nonadiabatic transition with an increasing N–O bond distance. Furthermore, it was verified that a 1,2-shift takes place in the pathway that results in the production of ketenimine, causing a nonadiabatic transition.

Introduction

The five-membered heterocyclic compound isoxazole is shown in Fig. 1(a). In organic synthesis, this kind of molecule is mostly employed as an inhibitor and finds utility in agrochemistry, anti-corrosion compounds, and medicines.[1–9] Since the 1960s, isoxazole's photochemical reactions have been researched. It is well known that the reaction is initiated by breaking the weak N2–O1 bond in the five-membered ring. The bond is broken to form a diradical, which is isomerized to 2*H*-azirine, and then the C3–C4 bond in the three-membered ring of 2*H*-azirine is broken to form oxazole.

Wakefield and Wright[11] pioneered the physicochemical characterisation of isoxazole and oxazole, together with the synthetic pathway, several reactions with electrophiles or nucleophiles, and the photolysis, thermal decomposition, fragmentation by electron impact, reductive bond-cleavage and so on were discussed in their paper. Furthermore, they summarised the quantum yield (%) of azirine derivatives based on the combination of functional groups located at R3, R4 and R5. Specifically, when R3 is a methyl group, R4 is hydrogen and R5 is a methyl group, the quantum yield is 14%;[12] when R3 is a phenyl group, R4 is hydrogen and R5 is an amino group, the quantum yield is 42%;[13] when R3 is a *para*-chlorophenyl group, R4 is hydrogen and R5 is an amino group, the quantum yield is 28%;[14] when R3 is a methyl group, R4 is hydrogen and R5 is a phenyl group, the quantum yield is 25%;[15] and it is 18%[16] when R3 is a phenyl group, R4 is a methyl group and R5 is an amino group. The quantum yield of azirine derivatives depends on the structure of the functional group. The n–π* electronic transition of azirine causes C3–C4 (N2–C4) bond-breaking and cyclization to oxazole (isoxazole).

In light of the experimental facts, a theoretical study was conducted in 1980. Tanaka *et al.*[17] clarified the energetics for the photoisomerization mechanism of isoxazole, with the photochemistry of 2*H*-azirine intermediate by *ab initio* MO–CI calculations. They found that the N2–O1 bond tends to loosen in the first singlet electronically excited state (S_1) upon the isomerization to 2*H*-azirine, and N2 and O1 have a negative net charge and lone electron pair, respectively, and repel each other due to electrostatic force. The subsequential internal

[a] *Graduate School of Science and Technology, Sophia University, Japan, Chiyoda, Tokyo 102-8554, Japan. E-mail: m-kimura-0o3@eagle.sophia.ac.jp*
[b] *Faculty of Science and Technology, Sophia University, Chiyoda, Tokyo 102-8554, Japan*

† Electronic supplementary information (ESI) available. See DOI: https://doi.org/10.1039/d4cp03137g

conversion (IC) to the ground state (S_0) results in the formation of a biradical on the N2–C3–C4 bond of the vinyl nitrene structure, which forms a new N2–C4 bond and obtains 2*H*-azirine. However, the N2–C4 dissociation of 2*H*-azirine proceeds by delocalising the electron density from the C atom of C5═O1, which has accumulated charge density to the antibonding orbital of the three-membered ring in S_1, ultimately causing the backward reaction to isoxazole. Furthermore, in the 2*H*-azirine to oxazole pathway, the removal of an electron from the non-bonding orbital of N promotes an increase in the C4–N2–C3 bond angle by changing the sp^2 hybridization orbitals to the sp hybrid. They also pointed out that this pathway to oxazole formation could occur in a single step, without any intermediates, when the intersystem crossing (ISC) between S_1 and the triplet state (T_1) happened.

Ab initio molecular dynamics (MD) simulations on 2-formyl-2*H*-azirine and isoxazole were performed by Cao for the first time in this story of isoxazole photochemistry,[18] in which Tully's fewest-switches surface hopping (FSSH) algorithm was employed.[19] One hundred classical trajectories were taken into account in the three-state-averaged complete active space (CAS) SCF (SA3-CASSCF) level with 12 electrons in 10 orbitals (12e, 10o) and a 6-31G* basis set, assuming two photoexcitations to S_1 and S_2. As a result, the forty trajectories in the 100 initiated isoxazole to S_1 produced 2-formyl-2*H*-azirine, and the nine trajectories converted to the minor product of 3-formylketenimine. Four trajectories of isoxazole were also found to dissociate back to the original isoxazole, and since the result was almost the same as the case when isoxazole was excited to the S_2 state, it is concluded that isomerization from isoxazole to oxazole does not occur. Other findings included the following: the lifetime of S_1 was determined to be 82.4 fs by fitting to a single exponential function, and the isomerization started at 2-formyl-*H*-azirine to oxazole was found only when excited to S_2.

In order to understand the ultrafast dynamics for ring-opening in heterocyclic systems, Geng *et al.*[20] using time-resolved photoelectron spectroscopy, which was supported by nonadiabatic *ab initio* MD simulation of isoxazole and oxazole in 2020. In their study, the molecules were excited by laser pulses at 200 nm, and the excited molecular dynamics were probed by those at 267 nm, while the ADC2 (the second-order algebraic-diagrammatic configuration scheme) theory was employed for their *ab initio* simulation with the aug-cc-pVDZ basis set. In particular, nonadiabatic transitions were taken into account through a surface hopping algorithm based on the Landau–Zener formula in their simulation. The simulation time was up to 100 fs after photoexcitation. Their measured ring-opening time of isoxazole was 35 fs, and their simulations also supported their own experimental result, with 80% of the trajectories undergoing N2–O1 dissociation within 100 fs. They also pointed out that the reaction rate initiated from oxazole was approximately two times slower and less efficient than the ring-opening product due to the presence of a small barrier after the photoexcitation.

On the other hand, Nunes *et al.*[10,21,22] investigated the photochemistry of 3,5-dimethylisoxazole matrix-isolated in argon at 15 K by the tunable UV-laser irradiation at 222 nm and infrared spectroscopy, with the theoretical support at the B3LYP/6-311++G(d,p) level. The existence of nitrile ylide was confirmed for the first time, and moreover, the reaction pathways were proposed as shown in Fig. 1(b). In their experiments, two different irradiation times were conducted for (a) 1 and (b) 80 minutes; each product was then isolated, and FTIR spectra were measured to confirm the azirine **3** and ketenimine **6** in the (a) case, while **3**, nitrile ylide **4**, and **6** in (b). It is also found that 3,5-dimethylisoxazole to 2,5-dimethyloxazole isomerization remains a minor event, but the oxazole **5** was produced by the subsequent irradiation to **4** at 340 nm light. The other isomerization process to **6** appeared involving the [1,2]-methyl shift. The mechanism of this 1,2-shift was discussed in 2002 by Wilsey *et al.*[23] at the CASSCF/6-31G* level; the shift of the vinylic hydrogen or carbon atom from the alkene to the carbene structure is attributed to the presence of a conical intersection between two electronic states. Carbene formation occurs directly from the π–π* state. However, the proposed reaction mechanism from isoxazole **1** to oxazole **5** was later disproved by Su[24] in 2016; the singlet potential energy surface (PES) was explored at the CASSCF and MP2-CAS (OVB-MP2, orthogonal valence bond Møller–Plesset second-order perturbation) level with the 6-311G(d) basis set. Three different pathways correlated with **5** were found from the Franck–Condon region of **1**, but the direct mechanism to **5** through the single conical intersection was concluded to be the most likely pathway from the viewpoint of both energetics and kinetics. They also performed experiments using Xe-matrix and found that the triplet ground state (T_1) was not involved in this isomerization mechanism.

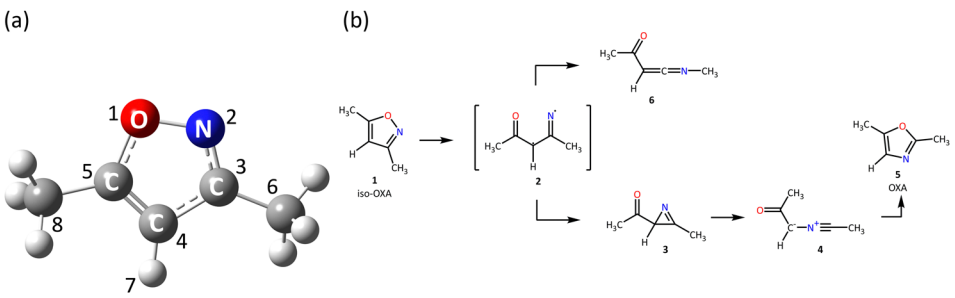

Fig. 1 (a) The equilibrium geometry of 3,5-dimethylisoxazole in the S_0 state at the XMS-CASPT2/cc-pVDZ + sp level and its label-number and (b) the isomerization process proposed by Nunes *et al.*[10]

In the present paper, non-adiabatic *ab initio* MD simulations were performed to explore the photoisomerization pathway from 3,5-dimethylisoxazole (iso-OXA) to 2,5-dimethyloxazole (OXA), considering the four lowest singlet electronic states (S_0, S_1, S_2, and S_3). In particular, the classical trajectory surface hopping (TSH) method based on the Zhu–Nakamura formula[25] was employed to take into account the nonadiabatic transitions. Two different *ab initio* methodologies were employed to obtain the potential energy and its gradient for the staying state of classical trajectory; one was the SA4-CASSCF method, and the other was the extended multi-state (XMS-) CASPT2 theory[26] to account for dynamical electron-correlation energy. For our basis sets, the Dunning cc-pVDZ + sp basis set[27] was mainly used, which is based on the cc-pVDZ function with diffusion functions for s-type and p-type orbitals widely used in aug-cc-pVDZ. Our simulations were performed up to 500 femtoseconds after photoexcitation. The three hundred classical trajectories evolved in time at the SA4-CASSCF level, while the fifty-two trajectories evolved at the XMS-CASPT2 level, and then these trajectories were analysed. The results successfully reproduced the various processes that have been discussed so far. In addition, the 1,2-shift transition process due to methyl groups was dynamically captured. Non-adiabatic transitions were identified as the cause of these methyl group shifts.

Methodology

The method for the *ab initio* electronic excited state calculation

We chose eleven molecular orbitals (MOs) in the active space at C_1 symmetry as shown in eqn (1) and used an active space that packs twelve electrons into it. In addition, the four electronic states were optimized with even weight in the SA4-CAS(12e, 11o)-SCF.

$$[(21a)\ (22a)\ (23a)\ (24a)\ (25a)\ (26a)\ (27a)\ (28a)\ (29a)\ (30a)\ (31a)] \quad (1)$$

In order to determine the most balanced theoretical approach for computational time and accuracy, we evaluated the vertical excitation energies around the Franck–Condon region using three different theories, the SA4-CASSCF, the XMS-CASPT2, and the symmetry-adapted cluster (SAC-) configuration interaction (CI) method. Furthermore, two different functions were used for the basis set; the aug-cc-pVDZ basis set was for SAC-CI, while cc-pVDZ + sp was for the SA4-CASSCF and XMS-CASPT2 methods. The sp function was extracted from the aug-cc-pVDZ. Since the SAC-CI theory is the closest to the full-CI approach among these methods, the obtained result was adopted as reference data for this system. The results are listed in Table 1 and Table S1 (ESI†). Note that the experimental value is estimated from the experimental conditions by Nunes *et al.*, which would not be the wavelength of the peak-maximum of the photoabsorption cross-section, although there is a difference of 0.49 eV between the experimental value and the SAC-CI calculation. The XMS-CASPT2 results could agree well with those by SAC-CI, but the SA4-CASSCF results show that each excitation energy is higher by about 0.5 eV. However, if considering the computation time, SA4-CASSCF was by far the quickest, as it took only about 1400 seconds, including the time to calculate the potential energy gradient. In contrast, the XMS-CASPT2 method required two processes in MPI parallel computing and took about 4000 seconds, where the used CPU was an Intel Xeon Gold 6330 (Ice Lake). Therefore, we focused on *ab initio* MD simulations based on the SA4-CASSCF method to reproduce the experimental evidence, while the simulations using the XMS-CASPT2 method were also conducted to confirm our results obtained by SA4-CASSCF where SA4-CASSCF with equal loads was performed and the level shift (0.7) option was used to avoid the intruder states. Almost all quantum chemical calculations were performed with the 2023.2 version of the quantum chemical calculation program package MOLPRO,[28] but the SAC-CI method only with Gaussian 16.[29] The calculations were performed for 8 months for XMS-CASPT2 and 4 months for SA4-CASSCF with a 12th Gen Intel(R) Core (TM) i7-12700K, 13th Gen Intel(R) Core (TM) i9-13900K, AMD Ryzen 9 7950X3D 16-Core Processor.

Nonadiabatic *ab initio* molecular dynamics simulation

Ab initio MD simulations were carried out, based on two different quantum chemical calculation methods, SA4-CASSCF and XMS-CASPT2 methods. The Wigner distribution functions[30,31] were used for initial coordinates and momenta given by the normal modes of molecular vibration in S_0; the vibrational frequencies were determined using harmonic oscillator analysis. In the simulations, for each case of SA4-CASSCF and XMS-CASPT2, these initial structures and momenta were generated using uniform random variables in the range of 0 to 1, resulting in three hundred and fifty-two different molecular configurations, respectively. The obtained initial structures and momenta were vertically excited from S_0 to S_1 following the Franck–Condon principle. The classical trajectories initiated with these initial conditions

Table 1 The vertical excitation energy (eV) and the squared values of transition dipole moment (TDM)

Electronic state	Primary electronic config. At the XMS-CASPT2 level	Theory				Exp.	$TDM^2/a_0{}^{2\,b}$
		XMS-CASPT2/ cc-pVDZ + sp	SA4-CASSCF/ cc-pVDZ + sp	SAC-CI/ aug-cc-pVDZ	SAC-CI/ cc-pVTZ		
S_1	Ryd $\leftarrow (\pi_{NO} + \pi_{CCC})^*$	6.53	6.73	6.26	5.93	5.77 (222 nm)	0.139
S_2	$\pi_{NO}{}^* + \pi_{CCC}{}^* \leftarrow (\pi_{NO} + \pi_{CCC})^*$	6.78	6.89	6.50	6.33	—	0.074
S_3	$\pi_{CONC}{}^* \leftarrow (\pi_{CO} + \pi_{CCN})^*$	7.14	7.54[a]	6.95	6.59	—	0.376

[a] The electronic configuration is different from XMS-CASPT2, see Table S1(a) (ESI). [b] Calculated at the XMS-CASPT2 level.

were propagated in time using a Velocity-Verlet integrator with a 0.25 fs time step. At each time step, the potential energy and its gradient were obtained by the direct *ab initio* calculation. On the way, when two potential energies are found to be lying closely to each other, the Zhu–Nakamura trajectory surface hopping (ZN-TSH) algorithm[25,32] is applied to make a nonadiabatic transition decision between the two electronic states; the non-adiabatic vector is obtained, and the transition along the vector is determined probabilistically at the pseudo-crossing by the ZN formula; the shapes of the two curvatures are evaluated, and the transition probability (p) is obtained from the crossing velocity. A random number (z) is generated between 0 and 1, and if the random number is less than the transition probability ($z \leqq p$), the running trajectory should hop to the other state. There are two different types of the non-adiabatic transitions, vertical hopping (VH) and non-vertical hopping (non-VH).[33,34] If the surface-hopping would happen, the momenta of the next step was adjusted following the ZN-TSH theory. In our ZN-TSH method, if the potential energy curves given by the sequential on-the-fly *ab initio* electronic state calculations generates an energy gap of $0.001E_h$ = 0.02721 eV = 219.5 cm^{-1} or more at each time step, we abort the *ab initio* MD run under those calculation conditions. The active space and the number of electronic states to be averaged were readjusted, and the entire simulation calculation was performed from the beginning. The final optimal active space and number of electronic states were 12 electrons and 11 orbitals, and 4 states. Regarding crashes during the simulation, one trajectory was observed in XMS-CASPT2 and two trajectories in SA4-CASSCF, but these trajectories were not counted, and these lost trajectories (one for XMS-CASPT2 and two for SA4-CASSCF) were compensated for by increasing the number of trajectories. This computational algorithm was repeated until the desired time was reached; our simulations were performed up to 500 fs after photoexcitation.

Results and discussion

Electronic state transition due to vertical excitation

The active MOs, which are also natural orbitals from SA4-CASSCF calculation in the S_0 equilibrium structure, are shown in Fig. S1 (ESI†). The 26*a* MO could correspond to a HOMO-like orbital for this system in CASSCF theory. In particular, the MOs of 24*a* to 29*a* are the key orbitals to describe the electronically excited states in SA4-CASSCF and XMS-CASPT2. The orbital properties are described below,

24*a*: anti-bonding orbital consisting of an out-of-plane bonding orbital composed of C5–O1 together with an out-of-plane bonding orbital of C4–C3–N2, $(\pi_{CO} + \pi_{CCN})^*$

25*a*: in-plane non-bonding orbital of N2 with a five-membered ring composed of C3–C4–C5–O1, $(n_N + \sigma_{CC+CO})^*$

26*a* (HOMO-like orb.): anti-bonding orbital consisting of an out-of-plane bonding orbital of N2–O1 with an out-of-plane bonding orbital of C3–C4–C5, $(\pi_{NO} + \pi_{CCC})^*$

27*a* (LUMO-like orb.): anti-bonding orbital consisting of an out-of-plane anti-bonding orbital of N2–C3 with an out-of-plane anti-bonding orbital of C5–O1, $(\pi_{NC}^* + \pi_{CO}^*)^*$

28*a*: Rydberg orbital around the C5 carbon atom, Ryd.

29*a*: anti-bonding orbital consisting of an out-of-plane bonding orbital of N2–O1 with an out-of-plane anti-bonding orbital of C3–C4–C5, $(\pi_{NO} + \pi_{CCC}^*)^*$where the atom labels are shown in Fig. 1(a).

Furthermore, Table S2(a) (ESI†) presents the expansion-coefficients of configuration state functions (CSFs) obtained at the XMS-CASPT2 level, whereas Table S2(b) (ESI†) shows those at SA4-CASSCF. The CI-coefficients for the S_0, S_1, and S_2 states had similar values and the same electron configuration at both levels, except S_3, which is of the single excitation of 24*a* → 27*a* at the XMS-CASPT2 level, but of 25*a* → 27*a* at SA4-CASSCF. The single excitation of 26*a* → 28*a* for S_1 results in a photoinduced electron transfer (PET) process from the bonding orbital of N2–O1 to the Rydberg orbital around the C5–carbon atom, which would be similar to the Rydberg orbital that appeared in the excited states of quinazoline,[35] but this PET process is not expected to be the direct cause of N2–O1 bond dissociation in the heterocyclic five-membered ring. The subsequent conformational change is thought to cause the electrons ionized in the cationic five-membered ring to transfer to the antibonding orbital and break the N2–O1 bond. We will discuss more detail on these mechanics later. The theoretical values for each vertical electronic excitation energy are listed for S_1, S_2, and S_3 in Table 1 and Table S1 (ESI†), where the experimental data was estimated from the experimental conditions by Nunes *et al.*

Nonadiabatic *ab initio* molecular dynamics with the ZN-TSH approach

The theoretical product ratios (%) are listed in Table 2, which also represent the dependency upon two different *ab initio* methodologies of SA4-CASSCF and XMS-CASPT2. As shown in the table, our theoretical results are in agreement with the

Table 2 The product ratios (%) for each compound

	Compound							
Theory	**1**	**3**	**4**	**5**	**6**	Other[a]	Excited state[b]	Total number of trajectories
XMS-CASPT2	9.6	55.8	3.8	1.9	3.8	11.5	13.5	52
SA4-CASSCF	3.7	56.3	0.7	0.0	3.3	33.0	3.0	300
Cao[18]	4.0	40.0	0.0	0.0	9.0	47.0	—	100
Nunes *et al.*[10]		Major	Minor	Minor	Minor			

[a] Trajectories that break the bond with isomers other than those described by Nunes *et al.* in Fig. 1(b). [b] Trajectories that remain in the excited state beyond 500 fs.

experimental results.[10] The formation of **6** was found to be low. This was because the classical trajectories that produced **6** did not remain in the stable structure of **6** and the methyl group bond to C2 was broken, causing dissociation. The data for the two comparisons were selected based on the criteria of experimental and theoretical conditions (gas phase), that are analogous to those employed in our own calculations.

The acquired relaxation times of the decay process are shown in Fig. 2(a) and (b). The fraction of trajectories was determined by the ratio of the number of trajectories staying in S_1 to the total number of trajectories. The theoretical lifetime was determined through the regression curve fitting of the relaxation data.[36] Initially, a single exponential function had been attempted, but it did not converge. Therefore, a bi-exponential function, eqn (2), was eventually utilized.

$$P(t) = P_0 + A\exp\left(-\frac{t - t_{\mathrm{lat}}}{t_{\mathrm{dec1}}}\right) + B\exp\left(-\frac{t - t_{\mathrm{lat}}}{t_{\mathrm{dec2}}}\right) \qquad (2)$$

The parameters t_{lat}, t_{dec1}, and t_{dec2} represent the latency and two decay constants, and the linear combination of the two exponential functions, listed in Table 3, has coefficients A and B.

Due to some trajectories trapped in excited states for a long time, the lifetime would become longer. When transitions to S_2 or S_3 happen, some did not reach the final product within 500 fs; P_0 is the ratio of the staying trajectories in excited states to the total trajectories. In the XMS-CASPT2 method, seven trajectories stay in the excited state even at 500 fs, in the SA4-CASSCF method, seventeen trajectories stay in the excited state. From this lifetime analysis, it was predicted that the $S_1 \rightarrow S_0$ transition could be classified into two categories, indicating the existence of two different decay processes.

Just after photoexcitation to S_1, the other transitions to S_2 frequently occurred at 36 of 52 trajectories, 33 VHs and 3 non-VHs in XMS-CASPT2, and 157 of 300 trajectories, 130 VHs and 27 non-VHs in SA4-CASSCF. These transitions occur because S_1 and S_2 could be in close vicinity around the Frank–Condon region. Some trajectories transitioned to S_3 or were trapped in S_2, but most quickly returned to the adjacent S_1 state and relaxed to S_0. The 143 of 300 trajectories hopped from S_1 to S_0 without going through S_2, all of which were VHs.

Table 3 Time constants for a bi-exponential function shown in eqn (2)

t_{lat}	t_{dec1}	t_{dec2}	P_0	A	B
(a) at XMS-CASPT2 level					
21.50	4.89	115.65	0.10	0.15	0.75
t_{lat}	t_{dec1}	t_{dec2}	P_0	A	B
(b) at SA4-CASSCF level					
14.70	10.77	119.81	0.01	0.19	0.80

$S_1 \rightarrow S_0$ transition mapping: nonadiabatic coupling homology in the Coulomb matrix framework

The relationship between the structures of VHs from S_1 to S_0 and the non-adiabatic transition probabilities was described using Coulomb matrices. The used data consisted of 300 classical trajectories in SA4-CASSCF, and the 366 structures and their probabilities that occurred within these trajectories were analysed based on machine learning by M. Rupp *et al.*, which dealt with modelling molecular atomization energies.[37]

Usually, Cartesian coordinates are used for MD simulations, but when treating molecular structure characteristics, Cartesian coordinates pose a problem; the same structure described after translation or rotation appears as a different structure. Therefore, Cartesian coordinates are transformed into the Coulomb matrix M defined by eqn (3) where $\{R_I\}$ is the Cartesian coordinate and $\{Z_I\}$ is

$$M_{IJ} = \begin{cases} 0.5Z_I^{2.4} & \text{for } I = J \\ \dfrac{Z_I Z_J}{|R_I - R_J|} & \text{for } I \neq J \end{cases} \qquad (3)$$

the nuclear charge of the I-th atom. As 3,5-dimethylisoxazole is a molecule consisting of 14 atoms, a 14 × 14 square matrix is constructed. By diagonalizing this matrix M, the eigenvalues

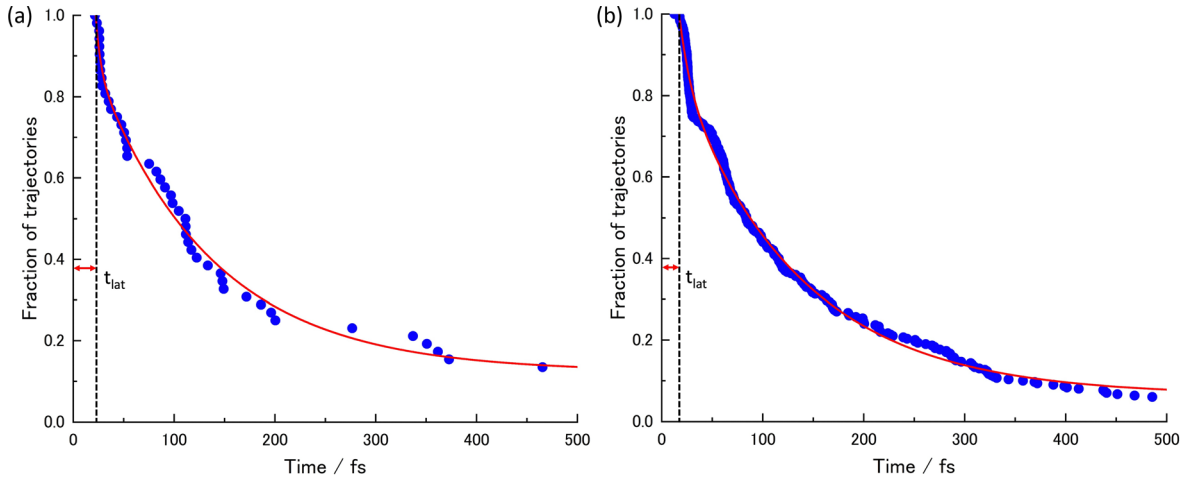

Fig. 2 The lifetimes of the S_1 state and the decay curves given by the regression curve fitting at (a) XMS-CASPT2 for 52 trajectories and (b) SA4-CASSCF for 300 trajectories.

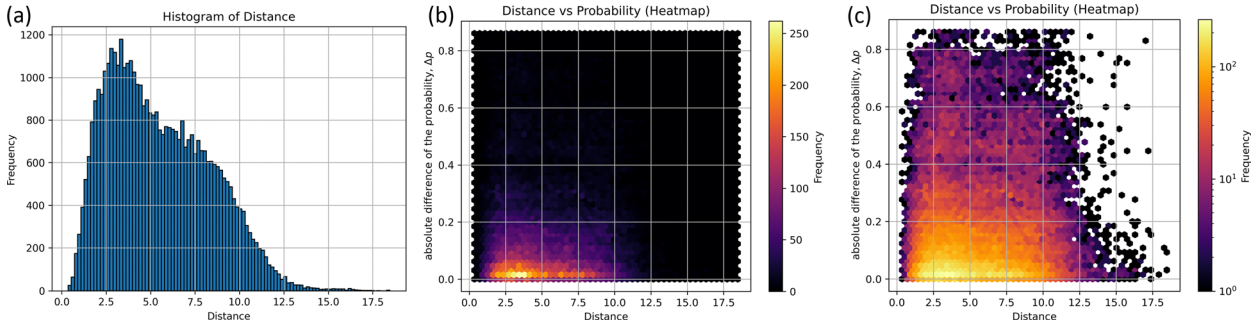

Fig. 3 The homology of non-adiabatic geometry and transition probability at the S_1 state; (a) the histogram for non-adiabatic geometry as a function of d-distance, (b) the heat map as a function of d-distance and absolute difference of the probability (Δp), and (c) the log scaled heat map for figure (b) is shown, where the width of the histogram is about 0.181.

and eigenvectors are obtained. These eigenvectors are arranged in descending order and are denoted by $\{\varepsilon\}$. The distance d was calculated by eqn (4) using $\{\varepsilon\}$ at two different structures.

$$d(M, M') = d(\varepsilon, \varepsilon') = \sqrt{\sum (\varepsilon - \varepsilon')^2} \qquad (4)$$

Since non-adiabatic transitions occurring within each fragmentation, such as methyl group dissociation, should be disregarded, the total number of employed structures amounts to 290.

The following two types of analysis were carried out.

(i) a comparison by brute force of structures with non-adiabatic transitions

$_{290}C_2$ = 41 905 possible ways

(ii) optimized structure in S_0 in contrast to non-adiabatic transition-undergoing structures

1 × 290 = 290 possible ways

The histograms on structural similarity (frequency) and heatmaps for differences in non-adiabatic transition probabilities (Δp) of different structures are shown in Fig. 3, where Δp is the absolute difference between the non-adiabatic transition probabilities of the two structures, and 97% of non-adiabatic transition probability-data have a probability greater than 0.4, as shown in Fig. 3(b).

The two peaks appear as clearly seen in the histogram. The maximum frequency of bin is 1179 at the distance d = 3.16, which implies that certain pairs of the structures corresponding to 3.16 exhibit the most probable pair in 290 non-adiabatic transitions. In particular, the five pairs of structures are illustrated in Table S3 (ESI†); the random.sample()[38] function was utilized to extract 1179 arbitrary combinations of five. The subsidiary peak was observed at d = 6.79 with the frequency of 797. It is also found that Δp is close to zero at d = 3.16 and 6.79 in Fig. 3(b). In other words, similar structures taking similar distances could take similar probabilities. However, it not easy to see the two peaks around d = 3.16 and 6.79 due to overlapping with other cases. To see the differences around d = 3.16 to 6.79, the heatmap of Δp scaled by the logarithm is drawn in Fig. 3(c). Δp at d = 3.16 is found to be scattered to 0.8, which means that some of them have the same distance but have different probabilities. The non-adiabatic transition probability is determined by including the potential gradient and the crossing speed at the pseudo-crossing of the two potentials, so it cannot be easily determined from the coordinates alone. However, the Δp distribution would suggest that there are two correlations at d = 3.16 and 6.79 between the structure of non-adiabatic transitions and transition probabilities.

The comparison-(ii) of the optimized structure in S_0 to the non-adiabatic structure provides the histogram and scatter plot presented in Fig. 4(a) and (b), respectively. Two peaks can be seen from the histogram result. The distance d at the highest frequency is 18.03 and the frequency at that time is 17, which indicates that the non-adiabatic transition occurred most frequently at d = 18.03 from the stable structure. The five arbitrarily selected structures at this distance are listed in Table S4(a) and (b) (ESI†). Another peak in Fig. 4(a) is observed around d = 9.98, with the frequency of 12; the non-adiabatic transitions occur in the regions closer than 18.03. In terms of probability, p, as depicted in Fig. 4(b), for d = 9.98 and 18.03, most probabilities are localized at 1.0 for both distributions, while the distribution at d = 18.03 extends to p = 0.20. Table S4(c) (ESI†) shows the results of the time-resolved histograms every 50 fs (or 100 fs).

In the $S_1 \rightarrow S_0$ non-adiabatic transition, these two types of emerged molecular structures could suggest the existence of two different lifetimes and two different conical crossings. Although there are exceptions in our classical trajectories, the shorter lifetime process corresponds to the lower peak (d = 9.98), while the longer lifetime process is associated with the higher peak (d = 18.03).

Trajectories back to the reactant/initial structure, isoxazole

There were five trajectories where the return process to the reactant occurred in the XMS-CASPT2 calculation. This happening would be slightly larger than the 4 trajectories out of 100 trajectories in the paper by Cao[18] considering three electronic states, S_0, S_1, and S_2. The time variation of the N2–O1 binding distance is shown in Fig. 5(a). The orange, blue, green, and purple lines correspond to trajectories staying in S_0, S_1, S_2, and S_3, respectively.

In four of the five trajectories, the bonding distance was greatly extended to 4.5 Å in the excited states by 200 fs, except in

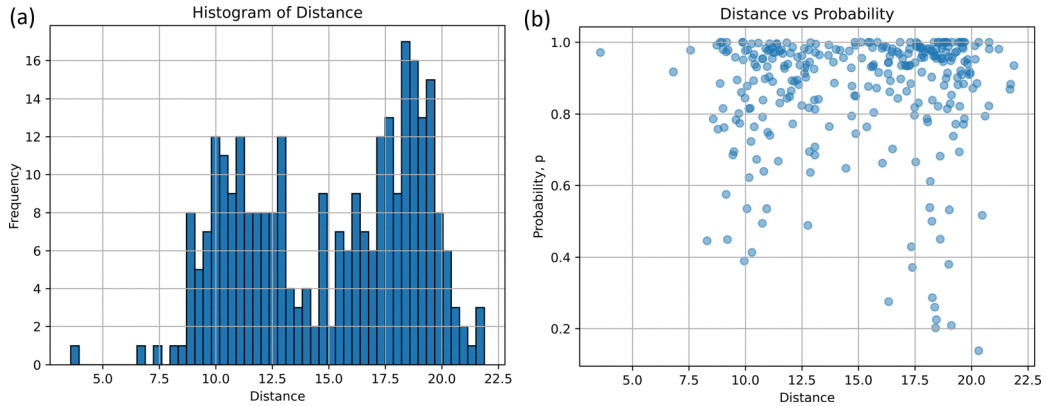

Fig. 4 The homology between the non-adiabatic geometry at S_1 and the S_0 equilibrium geometry, together with transition probability, p; (a) the histogram as a function of d-distance and (b) the scatter diagram as a function of d-distance and p are shown, where the width of the histogram is 0.366.

one trajectory, the N2–O1 bonding distance was not extended much. One of these four is deactivated to S_0 at 26 fs but continues to oscillate with large amplitude after 200 fs up to 300 fs. This motion is caused by the azirine structure it goes through. In addition to this trajectory, large amplitude vibrations are observed in the N2–O1 bond up to 5.0 Å in S_1. Finally, at 500 fs, all 5 trajectories become isoxazole structures and continue to oscillate stably. The $S_1 \rightarrow S_0$ non-adiabatic transition vector is shown in Fig. 5(b). This non-adiabatic vector indicates the N2–O1 bond direction, which contributes to N2–O1 bond formation and produces **1**.

The isomerization pathway to the azirine product

The azirine structure is shown in compound **3** in Fig. 1(b). This structure is the main product of the photoisomerization reaction of isoxazole. As mentioned above, isoxazole **1** is known to have two lifetimes. The estimated half-lives for the respective lifetimes are 24.89 fs and 101.66 fs at XMS-CASPT2. Here, the two classical trajectories with transitions at the times corresponding to these two half-lives are taken up in Fig. 6; the time variations for the potential energies and CI-coefficients shown along the classical trajectory where the nonadiabatic transition occurred at 23.50 fs are shown in Fig. 6(a) and (b), while those variations for the trajectory where the transition occurred at 104.75 fs are shown in Fig. 6(c) and (d). Time profiles up to 100 fs for the complexes in Fig. 6(b) and (d) are shown in Fig. S2(a) and S3(b) (ESI†). These two classical trajectories with the non-adiabatic transitions close to each other are typical phenomena. In the case of the transition at 23.50 fs, the electronic state immediately after photoexcitation is unstable as three electronic states can exist in close proximity, and within the first few fs the dominant electronic configuration becomes a single electron excitation of 26*a* → 28*a*, which involves the excitation from a HOMO-like orbital to a Ryd.-like orbital (or non-bonding orbital of C5–carbon, see Fig. S2, ESI†) (the blue line in Fig. 6(b), which is not unclear in this figure see Fig. S2(a) for an enlarged image, ESI†). However, this electron-rearrangement quickly happened due to a single-electron excitation from the HOMO-like orbital to the LUMO-like orbital (the orange line in Fig. 6(b)). The MOs of 26*a*, 27*a*, and 28*a* at 0 fs and 10 fs are listed in Table S5(a) (ESI†). This single electron excitation from the N2–O1 bonding orbital to the N2–O1 anti-bonding orbital leads to an unstable electron configuration and ultimately a longer N2–O1 bond distance at S_1. This dissociation of the N2–O1 bond causes the S_0 state to rise and a nonadiabatic transition between S_1 and S_0 occurs at

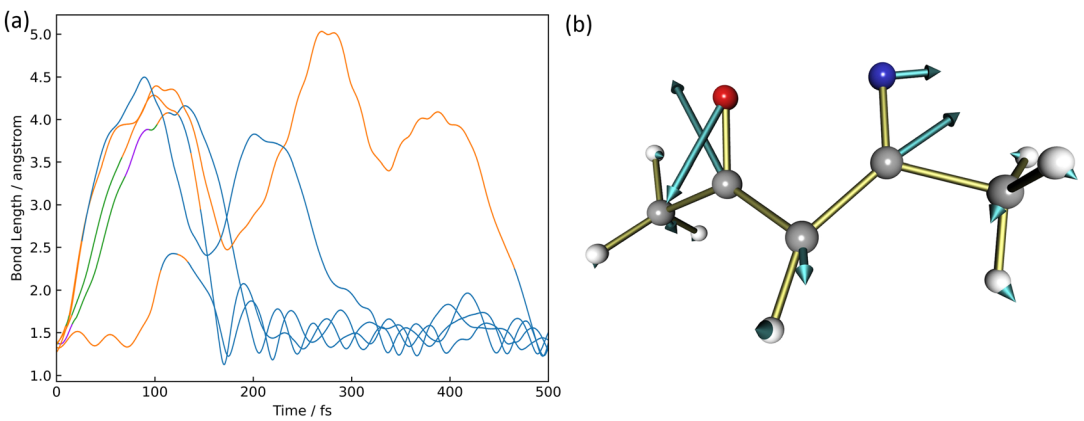

Fig. 5 The formation of 3,5-dimethylisoxazole, (a) the time variation of the N2–O1 bond length after photoexcitation to S_1 and (b) the relevant nonadiabatic vector between S_1 and S_0 where the blueline is S_0, orange is S_1, green is S_2, and purple is S_3.

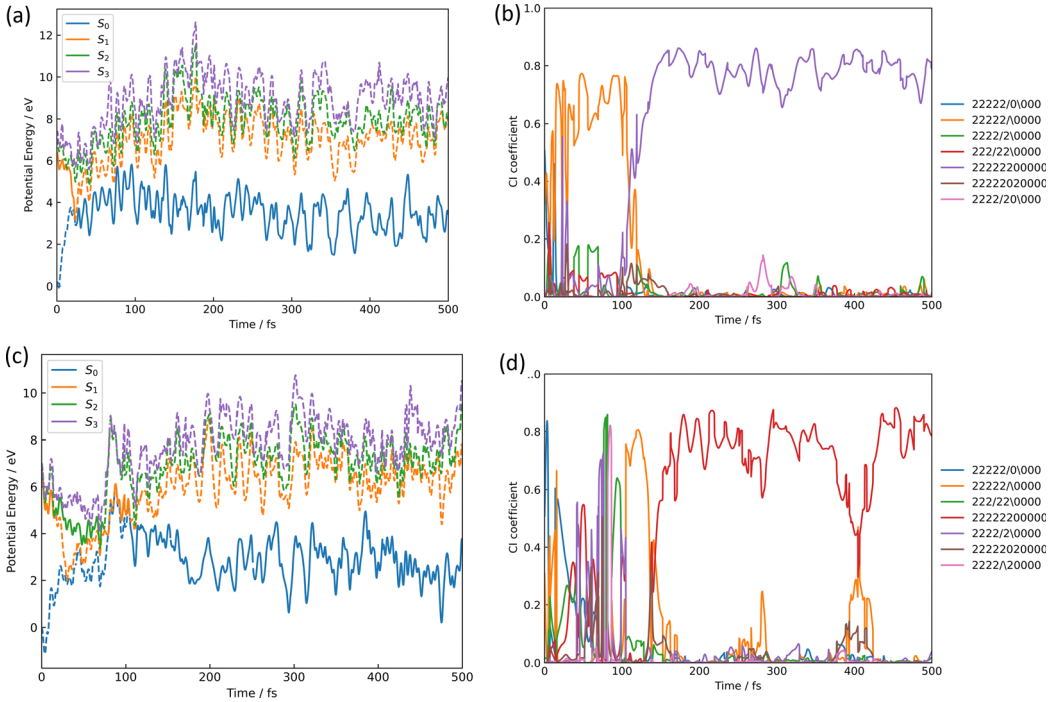

Fig. 6 The isomerization pathways to azirine by the two typical trajectories causing the $S_1 \rightarrow S_0$ transition at 23.50 fs for (a) and (b), while at 104.75 fs for (c) and (d); (a) and (c) are the potential energies of S_0, S_1, S_2, and S_3 over time-evolution, furthermore (b) and (d) are CI-coefficients over the same time. The legends used in (b) and (d) show how the 11 orbitals in the active space for CASSCF are packed with 12 electrons, with two "2" indicating two electrons occupied, the slash-symbol "/" indicating an alpha spin electron and the backslash-symbol "\" indicating a beta spin electron are packed, while zero "0" means an empty orbital, where the order of MOs in the active space is seen in eqn (1). Time profiles up to 100 fs for the complexes (b) and (d) are shown in Fig. S2(a) and (b) (ESI†).

23.50 fs. After the transition, in S_0, the single excitation of $26a \rightarrow 27a$ became the main configuration drawn by the orange line. This configuration kept this main structure until about 100 fs, and then (after 100 fs) the electronic structure started to be fully occupied up to the HOMO-like orbital drawn by the purple line. Furthermore, the time series of the MOs of $26a$ and $27a$ along the purple line of CI-coefficients in Fig. 6(b) in this period (18.75 fs to 250 fs) are shown in Table S5(b) (ESI†). After the non-adiabatic transition, the parent molecule (isoxazole) can no longer maintain a planar structure. The 1,3-diradical electronic structure appears on this time scale, which was proposed by Nunes *et al.*[10] In their study, open-shell singlet vinylnitrene **2** was assumed to be an intermediate molecule, and the photochemistry of isoxazole produced **3** and keteneimine **6**. Thus, the evidence for 1,3-diradical was also found in our simulation, 3,5-dimethylisoxazole **1**. Additionally, a typical classical trajectory for the second lifetime eventually experiences a non-adiabatic transition from S_1 to S_0 at 104.75 fs. However, prior to that, there are transitions from S_1 to S_2 at 15.5 fs, S_2 to S_1 at 68.25 fs, S_1 to S_2 at 69.75 fs, and S_2 to S_1 at 74.75 fs. Finally, at 79.5 fs, the trajectory relaxes from S_1 to S_0, but it suddenly returns to S_1 at 86.50 fs. The CI-coefficients show a mixture of many electronic states up to 100 fs in Fig. 6(d) (for more details, see Fig. S2(b), ESI†). Table S5(c) (ESI†) lists the MOs of $24a$, $25a$, $26a$, $27a$, and $28a$ until the final non-adiabatic transition occurs. Comparing these CI-coefficients with Fig. 6(d), the main electron configuration in the first few fs, as seen in the first trajectory, is a single electron excitation of $26a \rightarrow 28a$, involving the excitation from a HOMO-like orbital to a Ryd.-like (or C5–carbon non-bonded) orbital (blue line in Fig. 6(d)) moving to S_2 at 15.5 fs. Then, the CSF of $26a \rightarrow 27a$ replaces the main configuration, which is a single electron excitation from the bonding orbital of N2–O1 to the antibonding orbital. As a result, the N2–O1 bond breaks. Unlike the trajectory hopping at 23.50 fs, although the transition to S_2 is also involved, this trajectory hopping at 104.75 fs leads to the involvement of $25a \rightarrow 27a$ and $24a \rightarrow 27a$, which further elongates the N2–O1 bond length and distorts the planar structure. When the final non-adiabatic transition from S_1 to S_0 occurs at 104.75 fs, the structure is distorted from the planar structure and the N2–O1 bond length is larger than in the previous case. Within 50 fs after the final non-adiabatic transition, all electrons begin to be packed up to $26a$ as the main electronic configuration, and isomerization to azirine occurs quickly. These two structures appeared at the nonadiabatic transitions highlighting the similar trends to the trajectories classified by the Coulomb matrix, and the structural difference is thought to shorten the time of isomerization between the relaxation to S_0 and the formation of **3**. Furthermore, the dynamic processes of the molecular structure associated with

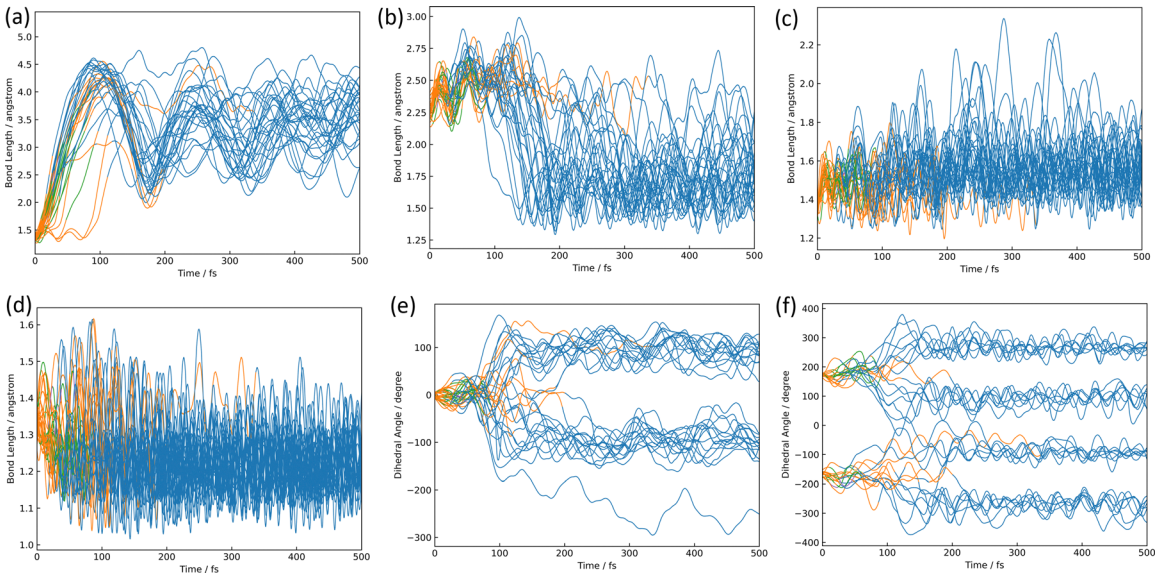

Fig. 7 The isomerization pathways to azirine; the time variations for (a) the bond length of N2–O1, (b) the bond length of C4–N2, (c) the bond length of C5–C4, (d) the bond length of C5–O1, (e) the dihedral angle of ∠C5–C4–C3–N2, and (f) the dihedral angle of ∠N2–C3–C4–H7, where the blueline is S_0, orange is S_1, green is S_2, and purple is S_3.

this isomerization are shown in Fig. 7(a)–(f) in terms of bond distances and dihedral angles. Fig. 7(a) clearly shows the dissociation of the N2–O1 bond immediately after photoexcitation. Multiple trajectories have similar directions of the N2–O1 bond dissociation and oscillate with similar periodicity to each other. Immediately after photoexcitation, the parent molecule undergoes a memorised molecular vibration in S_0 according to the Frank–Condon principle. This corresponds to vibrations up to R(N2–O1) = 1.5 Å and within 100 fs, indicated by the orange line, but as it undergoes a non-adiabatic transition to S_0, R(N2–O1) stretches to about 4.5 Å with a transition to the blue line, indicating a transition to S_0. This means that the parent molecule, 3,5-dimethylisoxazole **1**, which maintains the N2–O1 bond in S_0, loses this memory in the excited state and begins to vibrate with a high amplitude between N2 and O1. On the other hand, as shown in Fig. 7(b), after 100 fs, a corresponding vibration appears around R(C4–N2) = 1.7 Å, giving rise to a new C4–N2 bond; as there are multiple large-amplitude motions in the C4–N2 bond, the shape of the azirine triangle is not very stable, affecting the motion of the C5–C4 bond shown in Fig. 7(c). Precisely, it can be read that the distance between the C5–C4 bonds shrinks in S_1, but when hopping to S_0, the distance between the C5–C4 bonds increases and the stretching motion is more facilitated. This is because, in the stable structure of 3,5-dimethylisoxazole, this bond exhibits the properties of a double bond at S_0, but the N2–O1 bond dissociates at S_1 following the transition to S_0, thus weakening the properties of the C5–C4 bond, accompanied by a change in the dihedral angle. Nevertheless, while the aforementioned three stretching vibrations (N2–O1, C4–N1, C5–C4) are correlated, the C5–O1 vibration shown in Fig. 7(d), appears to oscillate stably like a spectator once the azirine molecule is formed. The C5–O1 bond is a type of resonance bond due to the five-membered ring on S_0. However, upon the N2–O1 bond cleavage during photoisomerization, a sp^2 hybridization of the C5–O1 bond emerges due to the bond being a fully double bond. The radical on the oxygen atom moves onto the carbon atom (C4) after the 1,3-diradical appears on the nitrogen and oxygen atoms.

Fig. 7(e) and (f) show the characteristics of the two dihedral angles that correlate mainly with the formation process of the azirine isomer of **3**. The dihedral angle of ∠C5C4C3N2 in Fig. 7(e) starts at almost 0° and remains in the molecular plane of isoxazole until the transition to S_0, after which the nitrogen atom moves out of the plane and becomes metastable at about 100°, giving rise to **3**. As in the previous discussion, the 1,3-diradical structure described by the single excitation of 26*a* → 27*a* after hopping to S_0 causes isomerization to **3**, a 3-membered ring. This photoisomerization finally produces diastereomers (*syn*- and *anti*-) and enantiomers (*R*- and *S*-) for **3**.

In our 500 fs simulations, the ratio of *syn*- to *anti*-form was eight to nineteen, with the *anti*-form being the major product. The experimental data is 58 to 42, which differs from our ratio, but it is noted that this ratio depends on the buffer gas used in the measurements.[14]

The time variation of the ∠N2C3C4H7 dihedral angle correlated to the mirror isomer is shown in Fig. 7(f); the dihedral angles are around 180° and −180° in S_1, but the angle shifts significantly from 180° to 100°, 260°, −100° and −260° after the relaxation in S_0. This conformational change occurs before the formation of the three-membered ring and determines which of the two pathways is the *R*- or *S*-conformational pathway. There is no bias towards either pathway, the ratio being approximately one to one.

The isomerization pathway to the products of nitrile ylide and oxazole

The structures of nitrile ylide and oxazole are shown in Fig. 1(b), nitrile ylide **4** and oxazole **5**. Immediately after the formation of azirine **3**, the dissociation of the C3–C4 bond gives rise to **4**. These three trajectories are referred to here as the *i*-, *j*-,

and *k*- trajectories, whereas two of the three trajectories (*i* and *j*) are products of the trapped nitrile ylide up to 500 fs. It is well known that **4** is easily formed from the *syn*-conformation of **3** with the further isomerization to **5**, because of the lower potential energy barrier than the *anti*-conformation.[10,24] The time profile of the potential energy for the *i*-trajectory is shown in Fig. S3(a) (ESI†). In addition, its CI-coefficients are shown in Fig. S3(b) (ESI†).

In one of the two trajectories producing nitrile ylide (*i*), the N2–O1 bond was dissociated immediately after photoexcitation, and the 1,3-diradical structure appeared (see Fig. 8(a)). The electronic structure mixing was quite like the previous discussion; the mixed configurations arose between the single excitation of 26*a* → 27*a* and the fully closed-shell structure until 100 fs (see Fig. S3(b), ESI†). Conversely, a commonality among the three trajectories is that the N2–O1 bond is dissociated following the transition to S_1. After the N2–O1 bond stretching, the C3–C4 bond also stretches (see Fig. 8(b)) as it begins to isomerize to **3**, forming **4**, which means that it does not spend much time staying in **3**, but soon becomes **4**. In other words, the time spent in azirine is not very long, and isomerization to nitrile ylide occurs immediately. The molecular orbitals of 26*a*, 27*a*, and 28*a* related to this process at 0.00 fs, 4.75 fs, 7.25 fs, and 7.50 fs are shown in Table S6(a) (ESI†). The main electronic structure is of a single electron excitation of 26*a* → 27*a* until the nonadiabatic transition to S_0 at 21.50 fs, but the structure changed to the single excitation of 26*a* → 28*a* from 4.75 fs to 7.25 fs, although it was very tiny period. This exchange of the 28*a* to 27*a* orbitals on the electronic transition indicates the S_2 state lying closely to S_1; the single-electron excitation of the HOMO-like orbital, 26*a*, to the Ryd-like orbital is dominant around the Franck–Condon region. While, at 7.50 fs, when the single electron excitation of 26*a* → 27*a* returns as the primary character, this Ryd-like orbital disappears and is replaced by the single electron excitation to the N2–O1 anti-bonding π orbital. It follows that the N2–O1 bonding distance increases; the transition to S_0 shows that the main electronic configuration features filling all MOs up to the HOMO-like 26*a* by two electrons, however the CI coefficient of a single electron excitation to 27*a* is also large up to around 100 fs. Therefore, the N2–O1 part of the 26*a* orbital looks like an out-of-plane bonding π orbital, whereas 27*a* is an anti-bonding π orbital, so the N2–O1 distance is considered to leave without bonding. Furthermore, this bond-breaking would widen the C5–C4–C3 angle, which would result in the formation of a bonding orbital of C4–N2, as can be read from the MOs at 76.00 fs; the MOs of 26*a* and 27*a* at 21.50 fs and 76.00 fs are shown in Table S6(b) (ESI†). As described above, **3** arose as an intermediate through the cyclization. However, after this cyclization, the C3–C4 bond was broken, resulting in the formation of **4**; this bond elongation began at around 175 fs in S_0. The time variation of MOs for 26*a* on the isomerization of **3** to **4** are shown in Table S6(c) (ESI†). In the process of nitrile ylide formation, the excess energy obtained in photoexcitation would be concentrated on the motion of the three-membered ring albeit of the energy redistribution to all motions of the molecule. Thus, the main pathway seems to have been in the direction of cleavage of the C3–C4 bond. The three trajectories (*i*, *j*, *k*) constitute a nitrile ylide, which then adopts both *syn*- and *anti*- forms as illustrated in Fig. 8(c) by the dihedral angle ∠N2C3C4C5. Subsequently, one of the nitrile ylide (*j*) adopts the *anti*-forms (∠N2C3C4C5 ≈ 180°), while the other and the oxazole former (*i*, *k*) adopt the *syn*-forms (∠N2C3C4C5 ≈ 360°).

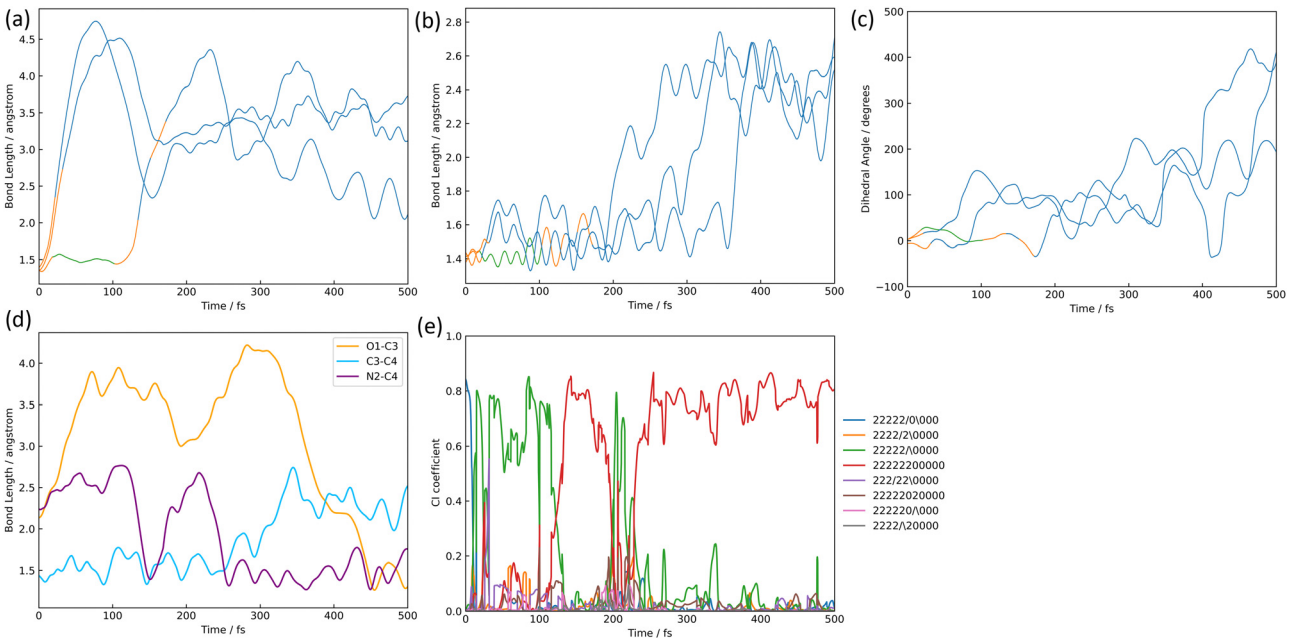

Fig. 8 The isomerization pathways to nitrile ylide and oxazole; (a) the bond length of N2–O1, (b) the bond length of C3–C4, (c) the dihedral angle of ∠N2C3C4C5 where the color lines correspond to the electric state mentioned in the figure caption of Fig. 7, (d) the bond length's alternation, and (e) the CI coefficients (the legends mentioned in Fig. 6) are shown over time-evolution.

Only one trajectory led to the isomerization from one of the three trajectories that formed **4** to **5**. As mentioned above, compound **4** has two isomers, the *anti*- and *syn*-form, in our simulation. Su also reported that two isomers could appear in the *ab initio* calculation;[16] it was stated that the only isomerized species to the *syn*-form would be isomerized to oxazole **5**. In our work, three trajectories of nitrile ylide were formed, and two of three trajectories were stable in the *anti*- and the *syn*-forms, respectively. One last trajectory underwent isomerization to oxazole after going through the *syn*-form. The trajectory that isomerized to **5** gave rise to a non-adiabatic transition from S_1 to S_0 at 31.75 fs, after which it formed azirine **3**. Thereafter, the C3–C4 bond begins to break after about 300 fs, while retaining the N2–C4 bond. When forming **3**, the conformation becomes a *syn*-form and maintains a *syn*-form when isomerized to **4**. The C4–O1 bond is formed immediately afterward, with a bond distance of 1.5 Å at 450 fs and stabilizes to **5**. The N2–C4, C3–C4, and O1–C4 bond distances are summarised as a function of time in Fig. 8(d), and the time variation of the CI-coefficients is shown in Fig. 8(e), where the coefficient of single-electron excitation of $26a \rightarrow 27a$ increases once at around 350 fs. Furthermore, the MOs from 350 fs to 425 fs from the formation of **4** to that of **5** are shown in Table S6(d) (ESI†). The single-electron excitation from the non-bonding orbital of C4 to the *anti*-bonding orbital of N2–C4 becomes dominant at this moment. Therefore, the C3–N2–C4 bond angle is expected to be distorted afterward. Finally, the main electron configuration is predominantly two electrons occupied up to 26*a*, and the bond between O1 and C4 is considered to stabilize.

The methyl migration to the product of 3-acetyl-*N*-methyl ketenimine

The product ratio of 3-acetyl-*N*-methylketenimine **6** is 3.8% in the XMS-CASPT2-based simulation, which is a minor event in terms of probability, but methylketenimine formation was found. In addition, a single other trajectory was observed in which the methyl group migrates once to form **6** as an intermediate, but the methyl group is subsequently cleaved off. In photoisomerization simulations of isoxazole, which is the backbone molecule of 3,5-dimethylisoxazole **1**, the formation of **6** has also been reported.[8] In that case, it was formed by a [1,2]-hydrogen shift. However, in our case, the methyl-group shift occurred at a smaller probability. On the trajectory for this pathway shown in Fig. 9(a), the hopping of the electronic state is roughly as follows; quickly after the photoexcitation, the molecule excited to S_1 at 0 fs made a non-adiabatic transition to S_2 at 16.75 fs and returned to S_1 again at 28.25 fs. It then transitioned again to S_2 at 55.75 fs and again to S_1 at 92.50 fs; the S_1 state lasted longer and transitioned to S_0 at 361.75 fs; the frequent switching between the S_1 and S_2 states is due to the proximity of the two states of 3,5-dimethylisoxazole **1** as mentioned before. In other words, vinylnitrene **2** does not undergo a nonadiabatic transition while it is close to S_0 at about 100 fs, but it does conduct several nonadiabatic transitions at the S_2–S_1 pseudo-crossing after it appears. When deactivated to S_0 in this structure of **2**, an azirine **3** is formed. In conclusion, the bifurcation points between **3** ($\rightarrow$ nitrile ylide **4** $\rightarrow$ oxazole **5**) and **6** depends on whether a nonadiabatic transition from the structure of **2** to S_0 occurs. The structural change of the molecule was also traced (see Fig. 9(b)). Immediately after excitation, the two dihedral angles ($\angle$O1C5C4C3 and $\angle$N2C3C4C5), which define the five-membered ring of the isoxazole skeleton, are near 0° until 100 fs, indicating that the five-membered ring structure was preserved. However, the five-membered ring structure gradually begins to collapse on S_1 after about 150 fs. At around 180 fs, *cis*–*trans* isomerization occurred in S_1; the dihedral angle of $\angle$O1C5C4C3 ($\angle$N2C3C4C5) began to increase (decrease), reaching around 100° (−100°) in S_1, resulting in a *trans* isomer. As soon as the $\angle$N2C3C4 bond shown in Fig. 9(c), the angle of the *trans* isomer, approaches 180° (or a linear shape), the MOs showing the methyl group and the N2–C3 bond easily interact, and the S_1 state comes close to S_0, resulting in a [1,2]-methyl shift as shown in Fig. 9(d), with a nonadiabatic transition to S_0, yielding **6**. In Table S7(a) (ESI†), the MOs associated with the formation of **6** are drawn at various time steps. Furthermore, the main electron configurations are listed in Table 4, together with the actual value of the coefficient for the CSF. Upon returning to S_1 at 92.50 fs, the electronic state is a single-electron excitation from the non-bonding orbital of oxygen (n_O) to the non-bonding orbital of nitrogen (n_N). This electronic configuration significantly differs from the configuration during the formation of **3** discussed in the previous section, because the azirine formation involves a one-electron excitation from the non-bonding orbital of carbon (n_C) to n_N. As mentioned above, in **3**, the two radicals on the N2 and O1 atoms moved onto the N2 and C4 atoms after a non-adiabatic transition from S_1 to S_0. On the other hand, in the pathway to ketenimine formation, there is a bi-radical on N2 and C4 atoms in the excited state, but they gradually start to move, and the bi-radical gather on the triangle formed by N2–C3–CH_3. Here, the migration structure on the triangle becomes the non-adiabatic geometry at the conical intersection as well and then a non-adiabatic transition occurs smoothly. The change in the molecular structure at this nonadiabatic transition to S_0 is as shown in Fig. 9(b); the $\angle$O1C5C4C3 is around 180° and the $\angle$N2C3C4C5 is around 0°, which indicates that the O1's dihedral angle opens further to 180° from 100° at *trans* isomer and the N2's dihedral angle returns from −100° to around 0°. Furthermore, a methyl shift starts to occur at this moment, resulting in a single electron excitation of $26a \rightarrow 27a$, which features the single electron excitation of π_{N-C4}^* to σ_{C3-Me}. After the transition to S_0, the electronic state becomes a ground state occupied with two electrons each up to 26*a*. There are two of fifty-two trajectories at XMS-CASPT2 with a methyl shift, both of which are in S_1 and undergo non-adiabatic transitions after the $\angle$O1C5C4C3 dihedral angle reaches around 180°. The MO after the transition is shown in Table S7(b) (ESI†). The N–CH_3 bonding orbital becomes larger as it moves towards the N2–CH_3 stable structure after the transition.

In order to understand the mechanism of the [1,2]-methyl shift associated with a nonadiabatic transition, the minimum energy

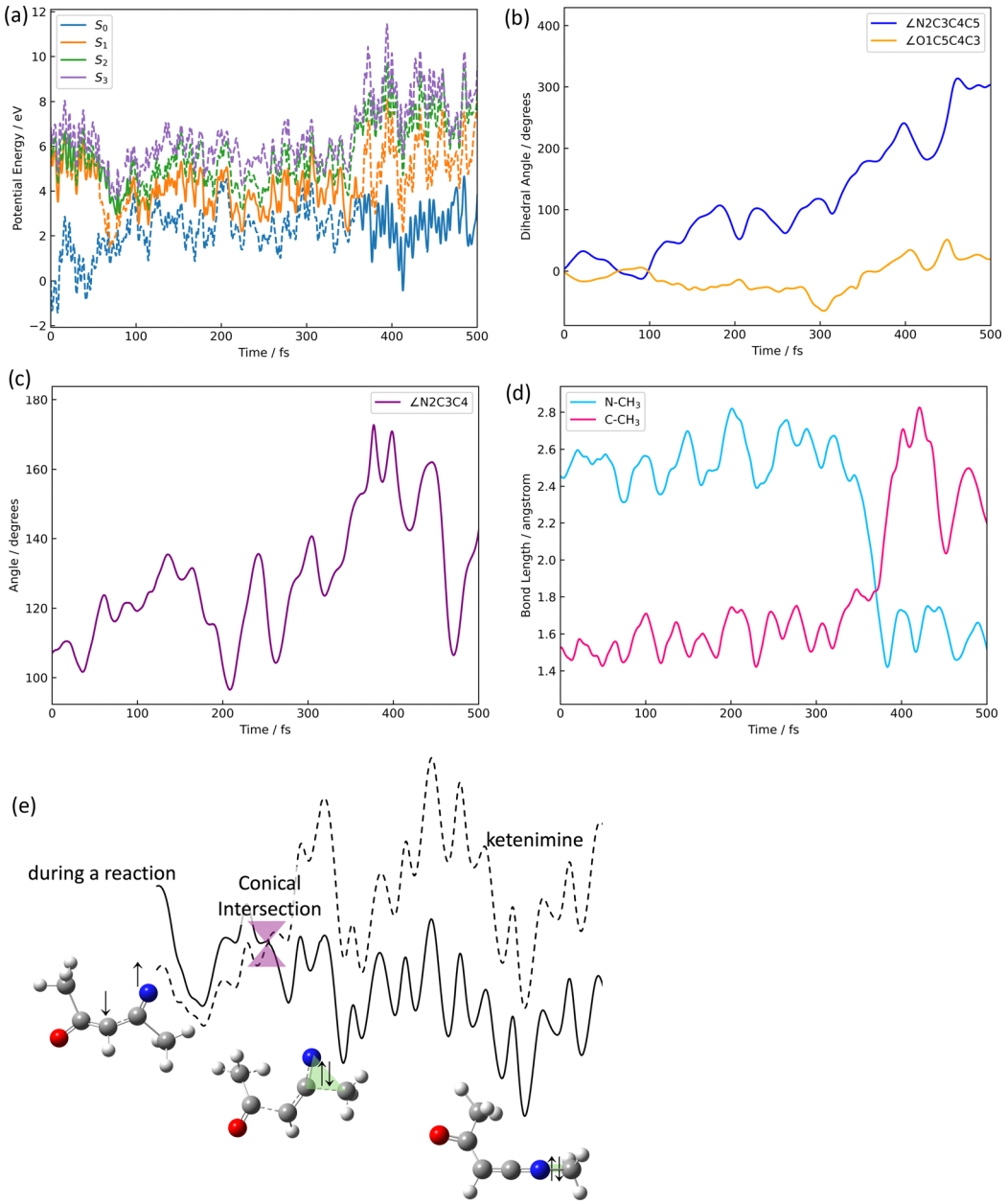

Fig. 9 The formation of ketenimine; the time variation for (a) potential energies over time, (b) the dihedral angle of ∠N2C3C4C5 and ∠O1C5C4C3, (c) the angle of ∠N2C3C4, (d) the bond length of methyl shift, and (e) the mechanism of 1,2-methyl shift.

Table 4 Electronic structures for the trajectory producing ketenimine

Time/fs	Single excitations	CI coefficients
0.00	$26a \rightarrow 28a$	0.93164482
16.75	$24a \rightarrow 27a$, $26a \rightarrow 28a$	0.45397086, 0.33661073
28.25	$26a \rightarrow 27a$	0.55543761
55.75	$26a \rightarrow 27a$	0.84249959
65.00	$26a \rightarrow 28a$, $25a \rightarrow 27a$	0.51832320, 0.44864707
92.50	$25a \rightarrow 27a$	−0.46944657
361.75	$26a \rightarrow 27a$	−0.79529092

structure for the conical intersection in S_1 was explored by using the trajectory-based geometry that actually caused the nonadiabatic transition along with the [1,2]-methyl shift. The optimized geometry at SA4-CASSCF shown in Fig. S4(a) (ESI†) was finally obtained in C_s symmetry; the bond distances for N2–CH_3 and C3–CH_3 are 2.107 Å and 1.699 Å, respectively. Thus, the bond distance to carbon (C3) is closer than that to nitrogen (N2) at the optimized structure for the conical intersection. The 26*a*, 27*a*, and 28*a* orbitals at this geometry are listed in Fig. S4(b) (ESI†), where the main electron configuration for S_1 is of the single-electron excitation of $26a \rightarrow 27a$. Since the 27*a* orbital features the σ antibonding orbital of N2–CH_3 (π_{N-CH_3}*), the σ bonding orbital of N2–CH_3 (σ_{N-CH_3}) has not appeared in S_1, yet. On the other hand, the coefficient of single electron excitation of $26a \rightarrow 28a$ is also large; the 28*a* features the π_{C3-N}* orbital, suggesting the possibility of the radical appearance on the top of nitrogen.

To clarify how the methyl group moves, the geometry when the carbon of the methyl group and the C3 and N2 atoms took a triangular structure was extracted from the data of classical trajectories with methyl shifts, and the MOs of 4*a*, 10*a*, 15*a*, 17*a*, and 24*a*, at that time are listed in Fig. S4(c) (ESI†). Besides, the MOs for the methyl radical alone are shown in Fig. S4(d) (ESI†). The ground state configuration for the methyl radical is as follows;

$$(1a)^2(2a)^2(3a)^2(4a)^2(5a)^1.$$

The comparison between Fig. S4(c) and (d) (ESI†) provided us the evidence for existing the methyl radical because of nearly identical orbitals occupied with electrons also appear in this system. This methyl group transfer mechanism appears to be equivalent to the reaction scheme of the hydrogen atom transfer mechanism found by Sarah *et al.* The scheme, adapted to the present system, is shown in Fig. 9(e). The 1,2-shift and the triangular structure of N2–C3–CH_3 are significant for this transfer mechanism. As shown in Table 2, the total product ratio of ketenimine is 3.8% (3.3%) at XMS-CASPT2 (SA4-CASSCF) including the *anti*- and *syn*-form. The optimization calculation was also performed to explore the most stable structure in S_0 for the ketenimine at XMS-CASPT2; the *anti*-form is staying at −0.949 eV, while the *syn*-form is at −0.945 eV in comparison to 3,5-dimethylisoxazole. Both forms could be energetically accessible in this photoisomerization. Actually, only two trajectories were correlated to the *anti*-form at XMS-CASPT2 without any *syn*-form, but seven (three) trajectories were correlated to the *anti*- (*syn*-) form at SA4-CASSCF.

The other products

The other complex products of 11.5% for XMS-CASPT2 and 33.0% for SA4-CASSCF were found, as present in Table 2. The complex products consisted of isomers and fragments resulting from the dissociation process. The four main complex products are listed in Table S8 (ESI†). To distinguish them from compounds **1–6**, fragments are designated **7**, **8**, **9** and **10**. As has been discussed above, all trajectories, except the two trajectories in the SA4-CASSCF method, undergo N2–O1 bond breaking immediately after photoexcitation. The subsequent dissociations happened in **7**, where the methyl group on the O side was cleaved (C5–C8); in **8**, where the methyl group on the N side was cleaved (C3–C6); in **9**, where acetonitrile was formed (C3–C4); and in **10**, where biradicals were formed (C4–C5). Table 5 gives details of the formation ratios together with Cao's results, and although there were few dissociation pathways in our simulation similar to Cao's results, methyl groups dissociated, and other isomers were identified.

Table 5 The other products (%)

	7	**8**	**9**	**10**	Other	Total
XMS-CASPT2	0	5.7	1.9	0	3.8	52
SA4-CASSCF	1.3	8	13.3	0.7	9.7	300
Cao[a]	0	0	26	14	7[b]	100

[a] Hydrogen terminated isoxazole. [b] Convergence problems.

Methyl group on the N side dissociation (8). The structural optimization was performed by releasing the methyl group. The ground state is dominated by a single electron excitation of 26*a* → 27*a*; the S_1 state corresponds to a single electron excitation of 25*a* → 27*a*. The MOs of 25*a*, 26*a*, and 27*a* are shown in Fig. S5(a) (ESI†). Since 27*a* is SOMO, which corresponds to 5*a* of the methyl radical, the state of this methyl group is the ground state.

There are two types of methyl group dissociation at both theoretical levels. One is that the ketenimine **6** formed but was not stable and then the methyl group was cleaved, while the other is that the methyl group dissociated directly. For example, at the SA4-CASSCF level, **6** was formed but was not stable, and in total eight trajectories involve methyl bond dissociation; five happened within 50 fs and three happened after 100 fs, 300 fs, and 400 fs, respectively. It is the S_1 state lying closely to S_0, which caused the instability of **6**. On the other hand, there are 16 trajectories at SA4-CASSCF, in which the direct dissociation happened just after the nonadiabatic transition to S_0. In other words, this conical intersection can also lead to the direct dissociation, as mentioned by Sarah *et al.* Furthermore, three trajectories show the direct dissociation in S_1 without hopping but then relax to S_0. The former is of the bond-cleavage in the ground state (D_0), but the latter is in D_1 and then hopping to D_0.

Producing acetonitrile (9). The forty-one trajectories produced acetonitrile at SA4-CASSCF and only one trajectory at XMS-CASPT2. The structure optimization was performed at SA4-CASSCF using the obtained molecular conformation at the dissociation limit assuming the two fragments distance to be 10 Å; both structures were optimized keeping the dissociation limit, where the C3–C4 bond was broken after relaxation to S_0 in 41 trajectories. The molecular orbitals of 23*a* and 26*a* are shown in Fig. S5(b) (ESI†). The HOMO is 26*a* in the system but 23*a* is the HOMO for acetonitrile. To make sure of our MO-assignment, the structure optimization for acetonitrile only was also performed, as shown in Fig. S5(c) (ESI†); the HOMO of acetonitrile alone is 11*a*, which corresponds to 23*a* in the system. In addition, the $OCCH_3CH$ fragment exhibited a 1,2-methyl shift in seven of the 41 trajectories at SA4-CASSCF. The shift occurred at the same time as the C4–C5 bond began to break after the non-adiabatic transition in six of seven. In the last one trajectory, the shift occurs about 200 fs after the C4–C5 cleavage. Table S9 (ESI†) shows the time variation of MOs for 26*a* and 27*a* from 24 fs to 100 fs. Following the time-profile of MOs, anti-bonding orbitals were obviously seen between the C3 and C4 atoms when focusing on 26*a*. In the MOs for 26*a* after 75 fs, furthermore a triangular bonding orbital is formed at the three points of C4–C5–C8 between the methyl group and the carbons that causes the migration, similar to the methyl migration described in the previous chapter. Note that no 1,2-methyl shift was confirmed at XMS-CASPT2.

Other minor dissociation pathways and isomerization pathways. In XMS-CASPT2, there was a three-body dissociation of CH_3 + CO + $CHCNCH_3$ and the formation of the bicyclic molecule; in SA4-CASSCF, there was an oxygen-containing

four-membered ring isomer, a single hydrogen dissociation of H7, and a NO molecule with the fragment.

Conclusions

In this study, we conducted non-adiabatic *ab initio* molecular dynamics simulations using the trajectory surface hopping method to elucidate the complex reaction dynamics in the photoisomerization of 3,5-dimethylisoxazole. We assumed photoexcitation from S_0 to S_1 due to zero-point vibrations and employed two different theoretical methods, XMS-CASPT2 and SA4-CASSCF, with the cc-pVDZ + sp basis set.

The isomerization pathway followed the route pointed out by Nunes *et al.* in their experiments, where the five-membered ring undergoes ring-opening after excitation to S_1 and subsequently undergoes non-adiabatic transition to S_0. After hopping to S_0, we identified pathways leading to the regeneration of isoxazole **1**, as well as the formation of azirine **3**, nitrile ylide **4**, oxazole **5**, and ketenimine **6**. Additionally, we calculated their quantum yields, revealing that **3** was the major product with a yield of 56%, successfully reproducing the experimental results.

By analyzing the time evolution of CI coefficients and molecular orbitals during the formation of **3**, we found that the bonding orbital between N2 and C4 emerges after hopping to the ground state, leading to the formation of the three-membered ring. In the case of **6** formation, we observed that the non-adiabatic transition occurs in a structure where the methyl group begins to shift, which corresponds to the 1,2-shift mechanism proposed by Wilsey *et al.*, successfully capturing this mechanism dynamically.

Notably, our theoretical simulations provide new insights into the excited-state lifetimes. For the XMS-CASPT2 method, two lifetimes of 4.89 and 115.65 fs were observed, while for the SA4-CASSCF method, lifetimes of 10.77 and 119.81 fs were identified. This revealed the existence of two distinct non-adiabatic transitions. Furthermore, using the Coulomb matrix, a tool frequently applied in machine learning, to analyze the S_1–S_0 non-adiabatic transition structures, we observed significant structural changes not only in comparison to the S_0 equilibrium structure but also under more forced conditions. Two distinct peak groups were discovered, suggesting that the non-adiabatic transition structures can be classified into two processes.

The findings of this study deepen our understanding of the photoisomerization mechanism of 3,5-dimethylisoxazole and provide new insights into non-adiabatic phenomena.

Author contributions

Mizuki Kimura: conceptualization, data curation, formal analysis, investigation, methodology, project administration, software, validation, visualization, writing – original draft. Shinkoh Nanbu: conceptualization, data curation, formal analysis, funding acquisition, investigation, methodology, project administration, resources, software, supervision, validation, visualization, writing – review & editing.

Data availability

The data that support the findings of this study are available from the corresponding author upon reasonable request. Additionally, the datasets generated and/or analyzed during the current study are available in the ESI.†

Conflicts of interest

There are no conflicts to declare.

Acknowledgements

This work was supported by Sophia University Special Grant for Academic Research, with Faculty of Science and Technology Proposal-based Research Fund.

References

1 X. Wang, Q. Hu, H. Tang and X. Pan, *Pharmaceuticals*, 2023, **16**, 228.
2 L. Zhou, Y. Zhang, R. Fang and L. Yang, *Mol. Catal.*, 2018, **460**, 27–35.
3 A. Khutorianskyi, B. Chalyk, P. Borysko, A. Kondratiuk and P. K. Mykhailiuk, *Eur. J. Org. Chem.*, 2017, 3935–3940.
4 M. A. Erteeb, F. Mahmoud and A. S. Kareem, *Int. Res. J. Pure Appl. Chem.*, 2022, **23**, 16–22.
5 A. Roua, A. Ameziane, E. Hassani, A. Fitri, A. T. Benjelloun, M. Benzakour, M. Mcharfi and K. Tanji, *J. Mol. Model.*, 2024, **30**, 193.
6 E. Elqars, A. Oubella, M. E. Hachim, S. Byadi, A. Auhmani, M. Guennoun, A. Essadki, A. Riahi, A. Robert, M. Y. A. Itto and T. Nbigui, *J. Mol. Liq.*, 2022, **347**, 0167–7322.
7 T. Morita, S. Yugandar, S. Fuse and H. Nakamura, *Tetrahedron Lett.*, 2018, **59**, 1159–1171.
8 J. Zhu, J. Mo, H. Lin, Y. Chen and H. Sun, *Bioorg. Med. Chem.*, 2018, **26**, 3065–3075.
9 M. Majirská, M. B. Pilátová, Z. Kudlicková, M. Vojtek and C. Diniz, *Drug Discovery Today*, 2024, **29**, 104059.
10 C. M. Nunes, I. Reva and R. Fausto, *J.Org. Chem.*, 2013, **78**, 10657–10665.
11 B. J. Wakefield and D. J. Wright, in *Advances in Heterocyclic Chemistry*, ed. A. R. Katritzky and A. J. Boulton, Elsevier Science, Amsterdam, 1981, vol. 25, ch. 4, pp. 1293–1298.
12 T. Sato and K. Saito, *J. Chem. Soc., Chem. Commun.*, 1974, **19**, 781–782.
13 T. Nishiwaki, A. Nakano and H. Matsuoka, *J. Chem. Soc. C*, 1970, 1825.
14 T. Nishiwaki and T. Saito, *J. Chem. Soc. C*, 1971, 3021.
15 B. Singh, A. Zweig and J. B. Gallivan, *J. Am. Chem. Soc.*, 1972, **94**, 1199.

16 T. Nishiwaki, T. Saito, S. Onomura and K. Kondo, *J. Chem. Soc. C*, 1971, 2644.
17 H. Tanaka, Y. Osamura, T. Matsushita and K. Nishimoto, *Bull. Chem. Soc. Jpn.*, 1981, **54**, 1293–1298.
18 J. Cao, *J. Chem. Phys.*, 2015, **142**, 244302.
19 J. C. Tully, *J. Chem. Phys.*, 1990, **93**, 1061–1071.
20 T. Geng, J. Ehtmaier, O. Schalk, G. W. Richings, T. Hansson, G. Worth and R. D. Thomas, *J. Phys. Chem. A*, 2020, **24**, 3984–3992.
21 C. M. Nunes, I. Reva, T. M. V. D. Pinho e Melo, R. Fausto, T. Solomek and T. Bally, *J. Am. Chem. Soc.*, 2011, **133**, 18911–18923.
22 C. M. Nunes, I. Reva, T. M. V. D. Pinho e Melo and R. Fausto, *J. Org. Chem.*, 2012, **77**, 8723–8732.
23 S. Wilsey and K. N. Houk, *J. Am. Chem. Soc.*, 2002, **124**, 11182–11190.
24 M. Su, *J. Phys. Chem. A*, 2015, **119**, 9666–9669.
25 T. Ishida, S. Nanbu and H. Nakamura, *Int. Rev. Phys. Chem.*, 2017, **36**, 229–285.
26 T. Shiozaki, W. Győrffy, P. Celani and H. Werner, *J. Chem. Phys.*, 2011, **135**, 081106.
27 T. H. Dunning Jr., *J. Chem. Phys.*, 1989, **90**, 1007–1023.
28 H.-J. Werner, P. J. Knowles, P. Celani, W. Györffy, A. Hesselmann, D. Kats, G. Knizia, A. Köhn, T. Korona, D. Kreplin, R. Lindh, Q. Ma, F. R. Manby, A. Mitrushenkov, G. Rauhut, M. Schütz, K. R. Shamasundar, T. B. Adler, R. D. Amos, J. Baker, S. J. Bennie, A. Bernhardsson, A. Berning, J. A. Black, P. J. Bygrave, R. Cimiraglia, D. L. Cooper, D. Coughtrie, M. J. O. Deegan, A. J. Dobbyn, K. Doll, M. Dornbach, F. Eckert, S. Erfort, E. Goll, C. Hampel, G. Hetzer, J. G. Hill, M. Hodges, T. Hrenar, G. Jansen, C. Köppl, C. Kollmar, S. J. R. Lee, Y. Liu, A. W. Lloyd, R. A. Mata, A. J. May, B. Mussard, S. J. McNicholas, W. Meyer, T. F. Miller III, M. E. Mura, A. Nicklass, D. P. O'Neill, P. Palmieri, D. Peng, K. A. Peterson, K. Pflüger, R. Pitzer, I. Polyak, P. Pulay, M. Reiher, J. O. Richardson, J. B. Robinson, B. Schröder, M. Schwilk, T. Shiozaki, M. Sibaev, H. Stoll, A. J. Stone, R. Tarroni, T. Thorsteinsson, J. Toulouse, M. Wang, M. Welborn and B. Ziegler, MOLPRO, version 2023.2, a package of *ab initio* programs, see **https://www.molpro.net**.
29 M. J. Frisch, G. W. Trucks, H. B. Schlegel, G. E. Scuseria, M. A. Robb, J. R. Cheeseman, G. Scalmani, V. Barone, G. A. Petersson, H. Nakatsuji, X. Li, M. Caricato, A. V. Marenich, J. Bloino, B. G. Janesko, R. Gomperts, B. Mennucci, H. P. Hratchian, J. V. Ortiz, A. F. Izmaylov, J. L. Sonnenberg, D. Williams-Young, F. Ding, F. Lipparini, F. Egidi, J. Goings, B. Peng, A. Petrone, T. Henderson, D. Ranasinghe, V. G. Zakrzewski, J. Gao, N. Rega, G. Zheng, W. Liang, M. Hada, M. Ehara, K. Toyota, R. Fukuda, J. Hasegawa, M. Ishida, T. Nakajima, Y. Honda, O. Kitao, H. Nakai, T. Vreven, K. Throssell, J. A. Montgomery, Jr., J. E. Peralta, F. Ogliaro, M. J. Bearpark, J. J. Heyd, E. N. Brothers, K. N. Kudin, V. N. Staroverov, T. A. Keith, R. Kobayashi, J. Normand, K. Raghavachari, A. P. Rendell, J. C. Burant, S. S. Iyengar, J. Tomasi, M. Cossi, J. M. Millam, M. Klene, C. Adamo, R. Cammi, J. W. Ochterski, R. L. Martin, K. Morokuma, O. Farkas, J. B. Foresman and D. J. Fox, *Gaussian 16, Revision C.01*, Gaussian, Inc., Wallingford, CT, 2016.
30 E. Wigner, *Phys. Rev.*, 1932, **40**, 749–759.
31 E. J. Heller, *J. Chem. Phys.*, 1978, **68**, 2066–2075.
32 The software is archived in "**https://pweb.cc.sophia.ac.jp/nanbu_lab/downloads.html**" with tar and gzip archive of "zntsh.tgz.".
33 H. Nakamura, *Nonadiabatic Transition Concepts, Basic Theories and Applications*, World Scientific, Singapore, 2012.
34 C. Zhu, K. Nobusada and H. Nakamura, *J. Chem. Phys.*, 2001, **115**, 3031–3044.
35 M. Motoyama, T.-H. Doan, P. Hibner-Kulicka, R. Otake, M. Lukarska, J.-F. Lohier, K. Ozawa, S. Nanbu, C. Alayrac, Y. Suzuki and B. Witulski, *Chem. – Asian J.*, 2021, **16**, 2087.
36 Origin(Pro), Version 2024. OriginLab Corporation, Northampton, MA, USA.
37 M. Rupp, A. Tkatchenko, K. Muller and O. A. Lilienfeld, *Phys. Rev. Lett.*, 2012, **108**, 058301.
38 Python Software Foundation. "random.sample." Python 3.10 Documentation, 2024, **https://docs.python.org/3/library/random.html**.

